Editors' Suggestion

Resonant interatomic Coulombic decay in HeNe: Electron angular emission distributions

A. Mhamdi,[1] F. Trinter,[2] C. Rauch,[2] M. Weller,[2] J. Rist,[2] M. Waitz,[2] J. Siebert,[2] D. Metz,[2] C. Janke,[2] G. Kastirke,[2] F. Wiegandt,[2] T. Bauer,[2] M. Tia,[2] B. Cunha de Miranda,[3] M. Pitzer,[1,2] H. Sann,[2] G. Schiwietz,[4] M. Schöffler,[2] M. Simon,[3] K. Gokhberg,[5] R. Dörner,[2] T. Jahnke,[2,*] and Ph. V. Demekhin[1,†]

[1]*Institut für Physik und CINSaT, Universität Kassel, Heinrich-Plett-Str. 40, D-34132 Kassel, Germany*

[2]*Institut für Kernphysik, J. W. Goethe-Universität, Max-von-Laue-Strasse 1, D-60438 Frankfurt am Main, Germany*

[3]*Sorbonne Universités, UPMC Université Paris 06, CNRS, UMR 7614, Laboratoire de Chimie Physique-Matière et Rayonnement, F-75005 Paris, France*

[4]*Helmholtz-Zentrum Berlin für Materialien und Energie, Division NP-ABS, Hahn-Meitner-Platz 1, D-14109 Berlin, Germany*

[5]*Theoretische Chemie, Physikalisch-Chemisches Institut, Universität Heidelberg, Im Neuenheimer Feld 229, D-69120 Heidelberg, Germany*

(Received 14 March 2018; published 16 May 2018)

We present a joint experimental and theoretical study of resonant interatomic Coulombic decay (RICD) in HeNe employing high resolution cold target recoil ion momentum spectroscopy and *ab initio* electronic structure and nuclear dynamics calculations. In particular, laboratory- and molecular-frame angular emission distributions of RICD electrons are examined in detail. The exciting-photon energy-dependent anisotropy parameter $\beta(\omega)$, measured for decay events that populate bound $HeNe^+$ ions, is in agreement with the calculations performed for the ground ionic state $X^2\Sigma^+_{1/2}$. A contribution from the $a^2\Pi_{3/2}$ final ionic state is found to be negligible. For the $He + Ne^+$ fragmentation channel, the observed laboratory-frame angular distribution of RICD electrons is explained by a slow homogeneous dissociation of bound vibrational levels of the final ionic state $A^2\Pi_{1/2}$ into vibrational continua of the lower lying states $X^2\Sigma^+_{1/2}$ and $a^2\Pi_{3/2}$. Our calculations predict that the angular distributions of RICD electrons in the body-fixed dipole plane provide direct access to the electronic character (i.e., symmetry) of intermediate vibronic resonances. However, because of the very slow dissociation of the $A^2\Pi_{1/2}$ state, the molecular-frame angular distributions of RICD electrons in the $He + Ne^+$ fragmentation channel are inaccessible to our coincidence experiment.

DOI: 10.1103/PhysRevA.97.053407

I. INTRODUCTION

Interatomic Coulombic decay (ICD) is a nonlocal electronic decay mechanism which is present in loosely bound matter. During ICD, an excess energy is transferred from excited species to their neighbors, and a slow electron is emitted. It has been predicted theoretically in 1997 [1] and verified experimentally a few years later [2,3]. Since this time, ICD has been extensively studied both theoretically and experimentally: (i) for different systems with increasing complexity and moving to exotic and small biological systems; (ii) with respect to complexity and variety of possible interatomic processes; and (iii) after being triggered by different excitation schemes, exciting particles, and detection methods. All those studies of ICD have demonstrated its generality in nature. A good overview of the theoretical and experimental achievements on ICD and a list of relevant references can be found in recent review articles [4–7].

Traditionally, experiments on ICD rely on the detection of charged particles (electrons and ionic fragments) produced by the decay. Usually, a coincident detection of those charged particles provides a clean fingerprint of ICD. Such measurements have a further important advantage: In many cases they allow an access to molecular-frame angular distributions (MFADs) of emitted electrons (see, e.g., Refs. [8,9] and references therein). This is particularly interesting, as laboratory- and molecular-frame electron angular distributions are very sensitive to an interplay of the emitted partial continuum waves and afford important complementary information on the dynamics of, e.g., the photoionization process, which may not even be accessible in the total cross sections [10].

At present, only little is known about angular distributions of ICD electrons. Reference [11] reports MFADs of ICD electrons measured after inner-valence ionization of Ne dimers. Joint experimental and theoretical studies of MFADs of ICD electrons released after inner-shell ionization and subsequent Auger decay of Ne dimers are reported in [12,13]. Here, an asymmetry in the dipole-plane angular distribution of ICD electrons with respect to the direction of detection of the doubly charged Ne^{2+} fragment suggests a scenario of localization of the K vacancy. In [14], MFADs of ICD electrons from He dimers were measured and interpreted within a simplified two-center-emission model. The latter work demonstrates a strong influence of the underlying nuclear dynamics on the angular emission distribution of ICD electrons.

In the present work, we study angular distributions of electrons released by resonant interatomic Coulombic decay (RICD) from HeNe [15–17], which is the smallest prototype system for the realization of a two-center resonant photoionization mechanism proposed in [18]. There, the role of an antenna

*jahnke@atom.uni-frankfurt.de
†demekhin@physik.uni-kassel.de

 ©2018 American Physical Society

is attributed to the He atom, whose $1s3p(^1P)$ excited state (at an energy of about 23.087 eV) lies already above the first ionization potential of Ne (21.564 eV) [19]. Experiments have demonstrated a considerable enhancement of the ionization rate of HeNe across the resonances [15]. In Ref. [15] it was possible to resolve the individual $3d\pi(v_r)$, $3d\sigma(v_r)$, and $3p\pi(v_r)$ vibronic states of the excited dimer and to measure their RICD mean lifetimes and relative excitation intensities. These measurements were interpreted by *ab initio* electronic structure and nuclear dynamics calculations [15,16].

The present manuscript is organized as follows: Details on the experiment are outlined in Sec. II. The RICD process in HeNe, an origin of the bound final ionic states $HeNe^+$, and a mechanism which results in a fragmentation of the dimer into $He + Ne^+$ are discussed in Sec. III. Section IV summarizes the present theoretical approach. In Sec. V A, the computed properties of He^*Ne states are compared to the experimental and theoretical results from Refs. [15,16]. Laboratory-frame angular distributions, computed and measured in this work for bound and fragmentation channels, are compared in Secs. V B and V C, while the theoretical predictions for the molecular-frame angular distributions in the fragmentation channel are reported in Sec. V D. We conclude in Sec. VI with a brief summary.

II. EXPERIMENT

A cold target recoil ion momentum spectroscopy (COLTRIMS) setup [20–22] was employed in order to investigate RICD of HeNe. The ion arm consisted of a 4-cm-long acceleration region. The electron arm of the spectrometer employed a Wiley-McLaren time-focussing scheme [23] incorporating an acceleration region of 6 cm length followed by a field-free drift region of 12 cm length. A full 4π solid angle of detection was achieved for ions with a kinetic energy up to 4.6 eV and electrons with kinetic energy up to 10 eV with this COLTRIMS analyzer. The HeNe dimers were produced by expanding a mixture of 80% He and 20% Ne through a precooled (51 K) nozzle with a diameter of 5 μm into vacuum. A set of two skimmers created a well-localized supersonic gas jet which was intersected by photons of beamline UE112_PGM-1 [24] at the synchrotron radiation facility BESSY II (Berlin) operated in single-bunch mode. Charged particles generated after excitation and RICD were guided by weak electric and magnetic fields to two time- and position-sensitive microchannel plate detectors equipped with delay-line anodes for position of impact encoding. By measuring the flight times and the positions of impact of each particle their initial vector momenta were deduced by reconstructing their trajectories inside the spectrometer in an offline analysis. All charged particles were measured in coincidence. The measured momenta yielded furthermore all derived quantities as kinetic energies or emission angles in the laboratory frame. From the latter, the relative emission angles were obtained employing the coincidence information. The photon energy resolution was found to be less than 1 meV.

The measured time-of-flight spectrum of the ions is depicted in Fig. 1(a). It demonstrates a clear separation of signals related to $^{20}Ne^+$ and the $^{22}Ne^+$ isotope. The events representing bound final ionic states $He^{20}Ne^+$ (labeled as "Bound") show a

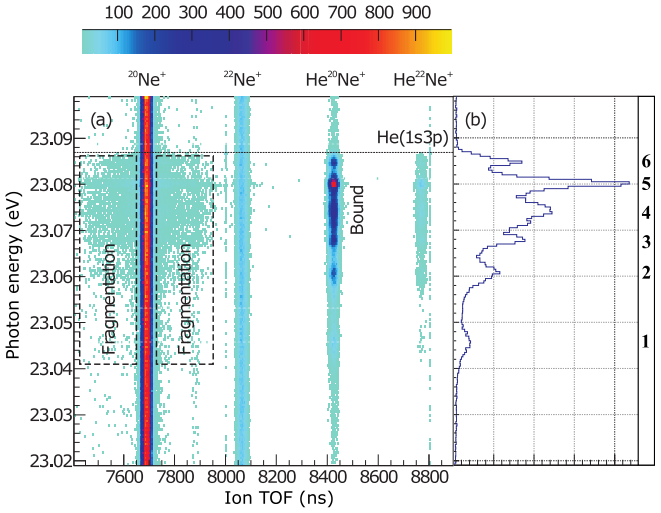

FIG. 1. (a) Measured time-of-flight spectrum of ions versus photon energy recorded in the vicinity of the $He(1s3p)$ resonance. Ionic signals marked as "Bound" and "Fragmentation" are due to the RICD in $He^{20}Ne$. (b) Excitation energy dependence of the $HeNe^+$ signal. Assignment of the resonances Nos. 1–6 is given in Table I.

strong enhancement of the ionization rate across the $3d\pi(v_r)$, $3d\sigma(v_r)$, and $3p\pi(v_r)$ resonances [15], which is caused by the antenna-receiver mechanism proposed in Ref. [18]. The features labeled as "Fragmentation" occur due to $^{20}Ne^+$ ions with kinetic energies below 100 meV [see Fig. 2(a)], which are visible as a halo to the strong line produced by the ionization of ^{20}Ne monomers in the gas jet. This dissociative signal is attributed to the $He + Ne^+$ fragmentation after the RICD electron emission, since it shows the same resonant enhancement as the signal of bound $HeNe^+$ states (see Fig. 4 in Sec. V). Figure 1(b) shows the enhanced $HeNe^+$ ion signal in more detail. As compared to Ref. [15], we were able to further increase the experimental resolution, which yields a more clear separation of the peaks arising from the excitation of the HeNe dimers into the $3p\pi(0)$, $3p\pi(1)$, and $3d\sigma(1)$ states.

III. THE RICD PROCESS IN HeNe

RICD of HeNe can be schematically represented as follows: Linearly polarized synchrotron radiation with a photon energy of $\hbar\omega$ excites the ground state of HeNe ("i") into different vibronic states of He^*Ne ("r"), which then decay via RICD into the final vibronic states of $HeNe^+$ ("f"):

$$\begin{aligned}
&\Omega_i v_i: \quad \mathrm{He}[1s^2]\mathrm{Ne}[2p^6] + \hbar\omega \rightarrow \\
&\Omega_r v_r: \quad \mathrm{He}^* \begin{bmatrix} 1s3d\pi\,^1\Pi \\ 1s3d\sigma\,^1\Sigma^+ \\ 1s3p\pi\,^1\Pi \end{bmatrix} \mathrm{Ne}[2p^6] \rightarrow \\
&\Omega_f v_f: \quad \mathrm{He}[1s^2]\mathrm{Ne}^+[2p^{52}\Pi/^2\Sigma^+] + \varepsilon\ell m\mu. \qquad (1)
\end{aligned}$$

Here, Ω is the projection of the total electronic angular momentum j on the molecular quantization axis, v stands for the wave function of the nuclear vibrational motion, and $\varepsilon\ell m\mu$ are the quantum numbers of the emitted partial electron waves in the asymptotical region [25,26] with the kinetic energy ε and

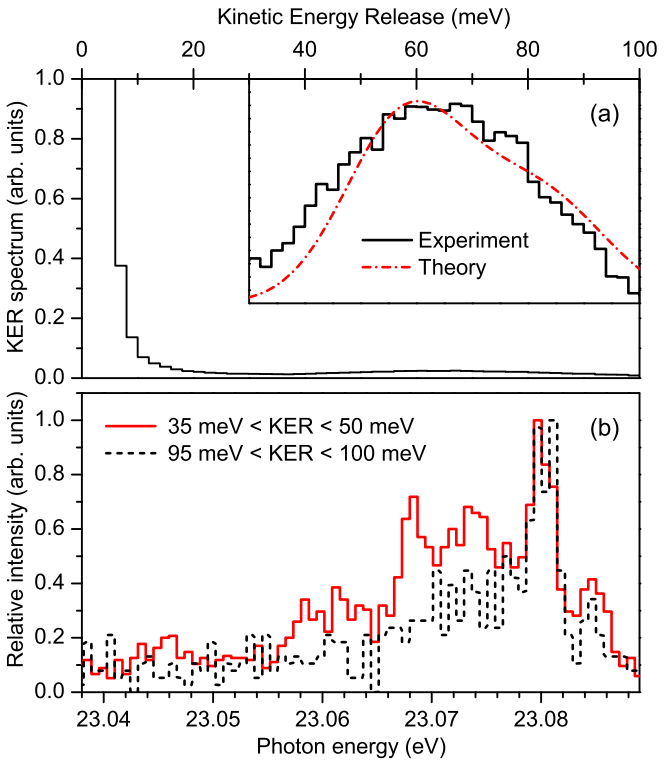

FIG. 2. (a) Experimental KER spectrum of the $^{20}Ne^{+}$ ions. The main signal, which peaks at a zero KER, is due to photoionization of monomers present in the gas jet. The weak shoulder between 30 and 100 meV represents ions produced by the He + Ne^{+} fragmentation subsequent to RICD. The individual contribution of the latter process, except a background signal due to ionized monomers, is shown in more detail in the inset. The dash-dotted curve in the inset shows the presently simulated KER spectrum. It is normalized to the maximum of the experimental spectrum and shifted by −5 meV to enable a better comparison with the experiment. (b) Relative number of counts for creation of He + Ne^{+} fragments with a kinetic energy release between 35 and 50 meV (solid curve) and between 95 and 100 meV (dashed curve) as functions of the photon energy in the range of the considered $He^{*}Ne$ resonances. Each curve is normalized to its maximum.

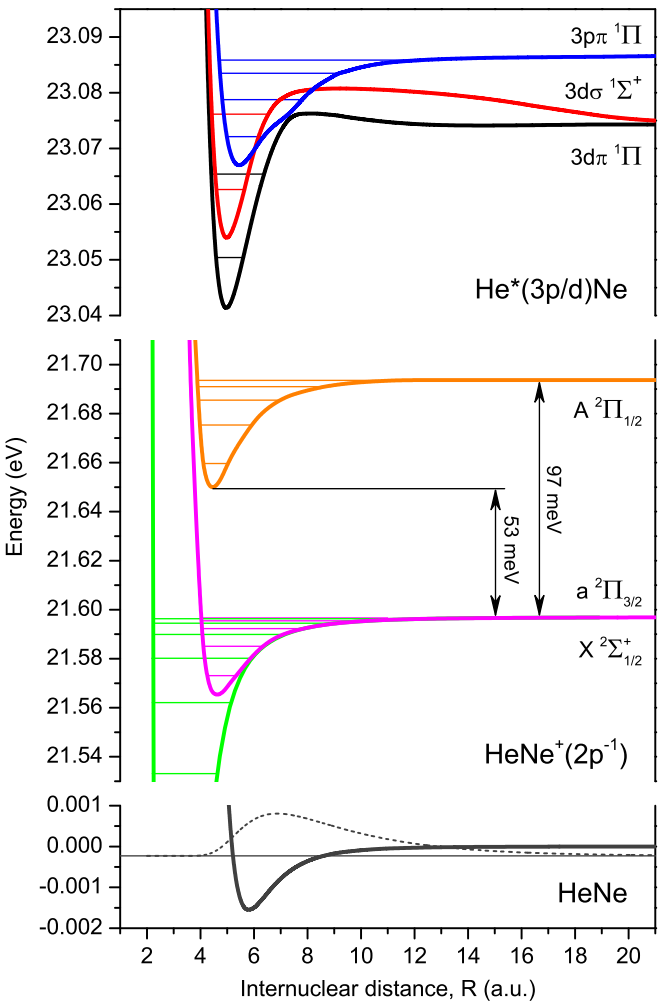

FIG. 3. Scheme of potential energies of the vibronic states relevant to RICD in HeNe. The depicted potential energy curves are taken from [15,16,27]. (Lowermost panel) The neutral electronic ground state of HeNe. The ground vibrational wave function of this state is depicted by the dashed curve. (Uppermost panel) The intermediate electronic $He^{*}Ne$ resonances (see assignment at the right). (Middle panel) The final $HeNe^{+}$ ionic states [see assignment at the right and also Eq. (2)]. In each panel, the energy positions of the relevant discrete vibrational states are indicated for each curve by the horizontal lines.

fixed projections m and μ of the orbital angular momentum ℓ and spin s, respectively. Potential energy curves of the relevant electronic states of the dimer from Refs. [15,16,27] are compiled in Fig. 3.

In the jj-coupling scheme, the total wave functions of the $X^2\Sigma^+_{1/2}$, $a^2\Pi_{3/2}$, and $A^2\Pi_{1/2}$ final ionic states of the process (1) read

$$|X^2\Sigma^+_{1/2}\rangle = \sqrt{\tfrac{2}{3}}\ |^2\Sigma^+_{\pm1/2}\rangle - \sqrt{\tfrac{1}{3}}\ |^2\Pi_{\pm1/2}\rangle, \quad (2a)$$

$$|a^2\Pi_{3/2}\rangle = |^2\Pi_{\pm3/2}\rangle, \quad (2b)$$

$$|A^2\Pi_{1/2}\rangle = \sqrt{\tfrac{1}{3}}\ |^2\Sigma^+_{\pm1/2}\rangle + \sqrt{\tfrac{2}{3}}\ |^2\Pi_{\pm1/2}\rangle. \quad (2c)$$

It is evident from the middle panel of Fig. 3, that all final ionic states (2a)–(2c) of the process (1) are bound [27]. Accordingly, one question immediately arises: Which final electronic state of the $HeNe^{+}$ ion produces the fragmentation signal observed in the time-of-flight spectrum in Fig. 1(a)? As one can see from the experimental kinetic energy release (KER) spectrum depicted in Fig. 2(a), the $^{20}Ne^{+}$ ions produced by fragmentation subsequent to RICD have kinetic energies within a range of 30–100 meV with a maximum located at approximately 65 meV. In addition, the total number of counts in the fragmentation channel [in the two rectangles in Fig. 1(a)] is quite comparable to that of the bound channel (the latter is only about three times larger than the former).

Obviously, this signal cannot be generated by a direct electronic transition to the dissociation continuum of these bound ionic states, as such a transition favors population of the vibrational states $\varepsilon_{v_f} > 0$ just above a dissociation limit. The KER spectrum of the electronic decay in the dissociation continuum of these ionic states is estimated to peak at zero with very small KER values well below 30 meV. In the experiment these very slow $^{20}Ne^{+}$ fragments overlap with the

dominant signal resulting from the ionization of monomers and are, therefore, inaccessible in the measured coincident data. Moreover, the presently estimated total probabilities for the population of all continuum and all discrete vibrational levels of these three final states, respectively, are about 5% vs 95%, which is in disagreement with the observation.

In order to clarify this issue, we turn to the energy diagram in Fig. 3. One can see that all discrete vibrational levels of the uppermost $A^2\Pi_{1/2}$ final ionic state (marked on the respective curve) lie between 53 and 97 meV above the dissociation limit of the lower states $a^2\Pi_{3/2}$ and $X^2\Sigma^+_{1/2}$. In other words, the complete manifold of rovibrational levels of the former electronic state is embedded in a bath of continuum rovibrational levels of the latter states. The respective ro-vibrational states with equal total angular momenta couple by nonadiabatic interaction through the nuclear kinetic energy operator [28]. The respective extremely slow dissociation mechanism is known in the literature as homogeneous dissociation [29,30].

The rationality of this assumption can be further substantiated by inspecting Fig. 2(b), which shows the photon energy dependence for creation of the $He + Ne^+$ fragments in two regions of KER. Selecting the KER region of 95–100 meV (dashed curve) results in a prominent peak at the energy of the highest vibrational level of the $3p\pi\,^1\Pi$ resonant state. This is a consequence of the Franck-Condon overlap between the vibrational wave function ($v_r = 3$) of this intermediate state with the highest vibrational level ($v_f = 4$) of the $A^2\Pi_{1/2}$ final ionic state, as both states extend to large values of R (see Fig. 3). In turn, the KER region of 35–50 meV corresponds to a population of the more confined and more tightly bound vibrational levels of the $A^2\Pi_{1/2}$ state, which have significant Franck-Condon overlap with all excited vibronic states. Consequently, the respective signal [solid curve in Fig. 2(b)] exhibits rich resonant structures due to RICD of these vibronic resonances.

IV. THEORY

Alternatively to the resonant ionization channel (1), each final vibronic state of the ion can be populated from the initial ground state via a weak direct photoionization channel $\Omega_i v_i \rightarrow \Omega_f v_f + \varepsilon\ell m\mu$. The total transition amplitude is thus given by the coherent superposition of the amplitudes of the direct and different resonant ionization pathways (atomic units are used throughout):

$$\begin{aligned} &D_k(\Omega_i v_i, \Omega_f v_f\, \varepsilon\ell m\mu) \\ &\quad = \langle \Omega_f v_f\, \varepsilon\ell m\mu | \mathbf{d}_k | \Omega_i v_i \rangle \\ &\qquad + \sum_{\Omega_r v_r} \frac{\langle \Omega_f v_f\, \varepsilon\ell m\mu | \mathbf{H^{ee}} | \Omega_r v_r \rangle \langle \Omega_r v_r | \mathbf{d}_k | \Omega_i v_i \rangle}{\omega - E_{\Omega_r v_r} + i\Gamma_{\Omega_r v_r}/2}. \end{aligned} \tag{3}$$

Here, $\mathbf{H^{ee}}$ and $\mathbf{d}_k$ are, respectively, operators for the electron-electron Coulomb interaction and dipole interaction of an electron with a photon of polarization k defined in the molecular frame ($k = 0$ for linear and $k = \pm 1$ for circular polarizations). The energies of the vibronic resonances and their total RICD widths are designated as $E_{\Omega_r v_r}$ and $\Gamma_{\Omega_r v_r}$, respectively, whereas the photon energy is related to the electron energy and the energy of final vibronic states via $\omega = E_{\Omega_f v_f} + \varepsilon$. It is worthwhile to notice that the summation over the index v_r in the right-hand-side of Eq. (3) describes the so-called lifetime vibrational interference (LVI, [31]), while the sum over the index Ω_r together with the direct ionization term is generally referred to as electronic state interference (ESI, [32]).

The total transition amplitudes (3) provide access to the angular distributions of emitted electrons. In the laboratory frame, they are parametrized by the total cross section $\sigma_{\Omega_f v_f}(\omega)$ for the population of a given final vibronic state $\Omega_f v_f$ and the respective asymmetry parameter $\beta_{\Omega_f v_f}(\omega)$ [33]. These two physical quantities can be computed via the following explicit equations [34,35]:

$$\sigma_{\Omega_f v_f}(\omega) = \sum_{\Omega_i \Omega_f} \sum_{\ell m \mu k} |D_k(\Omega_i v_i, \Omega_f v_f\, \varepsilon\ell m\mu)|^2, \tag{4a}$$

$$\begin{aligned} \beta_{\Omega_f v_f}(\omega) = {} & \frac{1}{\sigma_{\Omega_f v_f}(\omega)} \sum_{\Omega_i \Omega_f} \sum_{\ell m k} \sum_{\ell' m' k'} \sum_{\mu} (i)^{\ell+\ell'} \\ & \times (-1)^{\ell'+m+k} e^{i(\delta_{\ell m} - \delta_{\ell' m'})} \sqrt{30(2\ell+1)(2\ell'+1)} \\ & \times \begin{pmatrix} \ell & \ell' & 2 \\ 0 & 0 & 0 \end{pmatrix} \begin{pmatrix} \ell & \ell' & 2 \\ -m & m' & k-k' \end{pmatrix} \\ & \times \begin{pmatrix} 1 & 1 & 2 \\ k & -k' & m'-m \end{pmatrix} \\ & \times D_k(\Omega_i v_i, \Omega_f v_f\, \varepsilon\ell m\mu) \\ & \times D^*_{k'}(\Omega_i v_i, \Omega_f v_f\, \varepsilon\ell' m'\mu). \end{aligned} \tag{4b}$$

In these equations, summation over indices $\Omega_{i,f}$ has to be performed over all degenerate electronic states, $\delta_{\ell m}$ is the phase shift of the partial electron wave, and it is assumed that the spin of the electron μ is not resolved in the experiment. Finally, the total photoionization cross section (4a) can be set on the absolute scale by multiplying with the factor of $\frac{4\pi^2 \alpha a_0^2 \omega^{\pm 1}}{3 g_{\Omega_i}}$ (where α is the fine structure constant, the square of the Bohr radius $a_0^2 = 28.028$ Mb converts the atomic units for the cross section in megabarn, g_{Ω_i} is the statistical weight of the initial electronic state, and $\omega^{\pm 1}$ corresponds to the length or velocity gauge of the dipole transition operator $\mathbf{d}_k$).

The electronic parts of the total transition amplitudes (3) were computed employing the single center (SC) method and code [36–38]. The method has previously been applied to study excitation [39–42] and angle-resolved ionization of diatomic molecules [34,43–45], and even weakly bound dimers [9]. The center of the molecule was chosen in the middle of the two atoms. The SC expansions of occupied orbitals of HeNe included angular momenta with $\ell_c \leqslant 99$, while for the excited or ionized electron in the discrete or continuum spectrum it was restricted by partial harmonics with $\ell_\varepsilon \leqslant 39$. The calculations were performed in the relaxed-core Hartree-Fock approximation including monopole rearrangement of molecular orbitals [34,43–45]. The one-dimensional nuclear vibrational motion in the initial, excited, and final ionic states of HeNe was described by the theoretical approach described in [40,46], which includes underlying nonadiabatic effects in the He^*Ne excited states [16], using relevant data from Refs. [15,16,27]. Finally, the total transition amplitudes (3) were computed beyond the Franck-Condon approximation, i.e., the respective electronic transition amplitudes, obtained

TABLE I. Properties of the selected He*Ne vibronic states computed in the present work (SC) and in [16] within the nonadiabatic approximation, as well as the respective experimental data from Ref. [15].

Assignment		Energy (eV)		Width (meV)			Intensity (%)		
		Present, [16][a]	[15]	[16]	SC	[15]	[16]	SC	[15]
1	$3d\pi(0)$	23.0506	23.0460	3.74	5.73	5.0 ± 1.5	6.4	11.2	5
2	$3d\sigma(0)$	23.0633	23.0617	5.68	5.70	4.5 ± 1.0	6.0	9.4	13
3	$3d\pi(1)$	23.0655	23.0690	2.90	4.13	3.0 ± 1.0	15.0	14.1	10
4	$3p\pi(0)$	23.0722	23.0746	1.32	3.96	4.0 ± 1.5	0.5	1.1	38
	$3p\pi(1)$	23.0759		1.80	2.30		21.6	14.6	
	$3d\sigma(1)$	23.0768		3.66	3.51		19.4	12.4	
5	$3p\pi(2)$	23.0823	23.0806	1.00	1.67	2.5 ± 1.2	18.7	29.8	30
6	$3p\pi(3)$	23.0855	23.0851	0.42	0.59	$0.6^{+1.5}_{-0.3}$	12.4	7.4	4

[a]The computed energies and those from [16] coincide owing to the use of identical potential energy curves of He*Ne states.

at different internuclear distances, were integrated over the nuclear coordinate with the respective bra- and ket- vibrational wave functions in Eq. (3).

V. RESULTS AND DISCUSSION

A. Properties of the He*Ne vibronic states

Before analyzing the angular emission distributions of RICD electrons, let us briefly discuss the quality of the present electronic structure calculations. The energy positions, total RICD widths, and relative excitation probabilities of the selected He*Ne vibronic states computed in the present work are compared in Table I to corresponding theoretical and experimental data presented in [16] and [15], respectively. Since nuclear dynamics in the excited He*Ne states was treated here using potential energy curves from [16] (upper panel of Fig. 3), the presently computed vibronic energies (third column of Table I) coincide with those from [16]. As one can see, these computed energies slightly deviate from the experimentally observed energy positions of the He*Ne resonances [15] depicted in the fourth column. To enable a better comparison of the computed and the measured angle-resolved RICD spectra, the experimentally obtained resonance energies of the He*Ne vibronic states were used in the subsequent calculations via Eq. (3).

The computed total RICD widths of the individual He*Ne vibronic states (sixth column of Table I) agree within the uncertainties with the experimentally observed decay widths from [15] (seventh column). By comparing the fifth and the sixth columns of Table I one can see that the presently computed widths are on average by about 50% larger than those computed in [16]. Agreement between the presently computed relative intensities for the population of the individual He*Ne vibronic states and the experimentally [15] determined relative excitation intensities (ninth and tenth columns of Table I) is satisfactory. Note that the experimental relative intensity of 38% determined for peak No. 4 encompasses unresolved individual contributions from three vibronic states, as indicated by the brace in the second column of this table. It is difficult to judge, which of the two sets of the computed relative intensities, the one from [16] or the presently computed one, agrees better with the measured data set. For some resonances, intensities computed here and in [16] deviate from the respective experimental intensities by a factor of two.

We, finally, notice that the present calculations of the electronic properties of HeNe are performed within the one-

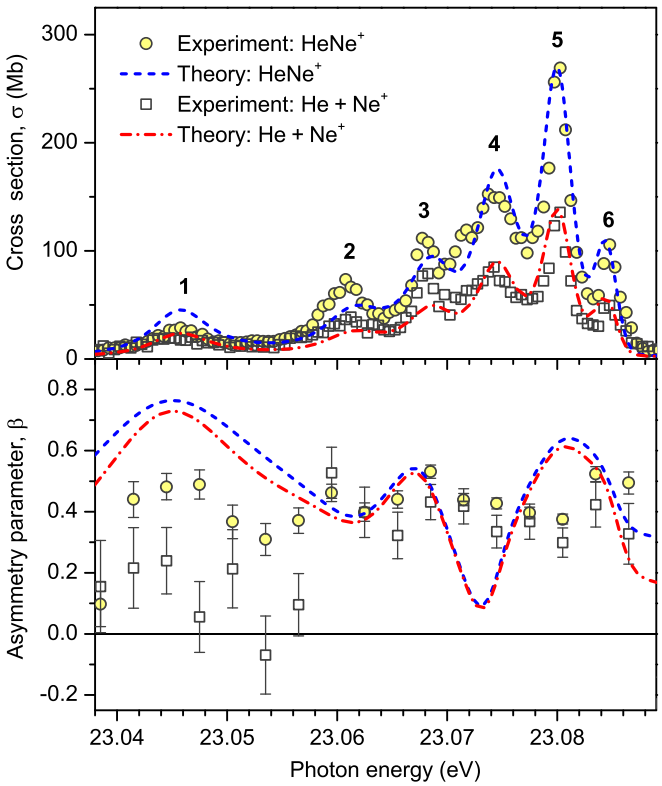

FIG. 4. Computed and measured photoionization cross sections (upper panel) and respective angular distribution parameters (lower panel) for the bound ($HeNe^+$) and fragmentation ($He + Ne^+$) channels as functions of the photon energy in the range of the considered He*Ne resonances. The enumeration of the peaks corresponds to that used in Table I. The theoretical data (curves) are additionally broadened by the experimental photon energy resolution. Experimental cross sections (symbols) are normalized to the present theory at their maxima, and the respective uncertainties (not shown) are smaller than the size of the symbols. No further normalization for the experimentally obtained β parameter (symbols with error bars) is required.

particle Hartree-Fock approximation for the excited and ionized electron. We thus neglected effects of correlations between the emitted electron and the ionic core, which are incorporated in the theoretical approach used in [16]. This is the main reason for the difference between the two sets of computational results in Table I.

B. Laboratory-frame angular distributions for the $HeNe^+$ channel

We first analyze the laboratory-frame angular distribution of the RICD electrons belonging to bound $HeNe^+$ final states. The respective experimental cross section $\sigma(\omega)$ and anisotropy parameter $\beta(\omega)$ are depicted in Fig. 4 by open circles as functions of the exciting-photon energy across the range of considered He*Ne resonances. The computed $\sigma(\omega)$ and $\beta(\omega)$ for this channel are also depicted in Fig. 4 by dashed curves. The latter include contributions from all bound vibrational levels of the $X^2\Sigma^+_{1/2}$ and $a^2\Pi_{3/2}$ electronic states of the $HeNe^+$ ion, which are defined by Eqs. (2a) and (2b), respectively (see also middle panel of Fig. 3).

One should stress that the main contribution ($\approx$98%) to the theoretical spectrum of the bound channel is provided by the electronic decay into the $|^2\Sigma^+_{\pm1/2}\rangle$ basis state. This is because the computed partial RICD widths of this basis state are almost two orders of magnitude larger than those of the $|^2\Pi_{\pm1/2}\rangle$ and $|^2\Pi_{\pm3/2}\rangle$ basis states. This can be explained by the fact that the $|^2\Sigma^+_{\pm1/2}\rangle$ state is populated by the ionization of the $2p_z$ orbital of the Ne atom. This orbital points towards He, which is the source of a virtual photon in ICD. In other words, the respective Coulomb matrix elements $\langle 1s_{\rm He},\varepsilon_{\rm RICD}|\mathbf{H^{ee}}|R,2p_{\rm Ne}\rangle$ for the decay of each resonance $R=\{3d\pi,3d\sigma,3p\pi\}$ are much larger for the $2p_z$ orbital of Ne, than those for $2p_{x,y}$ orbitals.

The upper panel of Fig. 4 illustrates a good quantitative agreement between the computed (dashed curve) and the measured (open circles) cross sections of the bound channel. As one can see, the absolute values of the computed asymmetry parameter are very similar to the measured ones. However, variations of the computed $\beta(\omega)$ across the vibronic resonances (enumerated in the upper panel) are somewhat different from those seen in the measured $\beta(\omega)$ (cf., open circles and dashed curve in the lower panel of Fig. 4). The latter variations emerge as a consequence of LVI and ESI effects [34,43–45]. Both interferences are known to be very sensitive to the quality of calculation of the total transition amplitudes (3). This is the main reason for a disagreement between the theoretically obtained $\beta(\omega)$ and the measured ones.

For instance, the present calculations overestimate the excitation intensity of resonance No. 1 (see first line in Table I). As a consequence, a relative contribution of the resonant channel across this peak is inappropriately enhanced, which results in slightly larger values of the computed $\beta(\omega)$. In addition, peak No. 4 consists of three unresolved resonances (see assignment in Table I). Both LVI and ESI are extremely sensitive to the energy positions of those overlapping resonances. As was mentioned in the preceding subsection, the respective energies were set in the calculations to the experimental position of peak No. 4. This can be a reason for the slightly different dispersion of the computed and the measured $\beta(\omega)$ in the energy range across this peak.

C. Laboratory-frame angular distributions for the $He + Ne^+$ channel

In order to verify the assumption on the origin of the $He + Ne^+$ fragmentation channel, we estimated the KER spectrum for the $A^2\Pi_{1/2}$ state Eq. (2c). The present calculations unveil that a RICD transition into this final ionic state populates mainly its bound vibrational levels. These are located between 53 and 97 meV above the lowest dissociation limit (see middle panel of Fig. 3). The probabilities of the population of all vibrational levels of the $A^2\Pi_{1/2}$ state can be considered as an estimate of the respective KER spectrum by assuming their subsequent homogeneous dissociation in the limit of the $X^2\Sigma^+_{1/2}$ and $a^2\Pi_{3/2}$ states. The computed population probabilities, convoluted with a broadening function of 15 meV FWHM to simulate rotational level distributions in each vibrational state and an experimental kinetic energy resolution of the detected fragments, are depicted in the inset of Fig. 2(a) by a dash-dotted curve. Although the present theory predicts slightly higher kinetic energies of the fragments (note that the computed spectrum was shifted by -5 meV), it basically explains the observation of $^{20}Ne^+$ ions in the kinetic energy range of 30–100 meV. The implied shift suggests a somewhat deeper minimum in the potential energy curve of the $A^2\Pi_{1/2}$ state.

The angle-resolved RICD spectra measured for the fragmentation channel ($He + Ne^+$) and computed for the $A^2\Pi_{1/2}$ state Eq. (2c) are depicted in Fig. 4 by open squares and dash-dotted curves, respectively. Interestingly, the cross sections $\sigma(\omega)$ and the asymmetry parameters $\beta(\omega)$ measured for the bound (open circles) and the fragmentation (open squares) channels possess very similar exciting-photon energy dependencies. This observation is perfectly reproduced by the present calculations (cf. dashed and dash-dotted curves in each panel of Fig. 4). This is because the main contribution to the RICD transition populating the final ionic states Eq. (2) is provided by the $|^2\Sigma^+_{\pm1/2}\rangle$ basis state, which governs the ICD electron angular emission distributions in both channels. A visible difference between the $\beta(\omega)$ computed for the two channels is due to small contributions of the $|^2\Pi_{\pm1/2}\rangle$ and $|^2\Pi_{\pm3/2}\rangle$ basis states to the final ionic states (2).

A dominant contribution of RICD transition in the $|^2\Sigma^+_{\pm1/2}\rangle$ basis state explains also rather comparable integral intensities observed for the bound and the fragmentation channels. In the theory, they relate as approximately 2:1, as is dictated by the admixtures of the latter basis state to the total wave functions (2a) and (2c). Experimentally, the former channel is about three times stronger than the latter (note that the experimental cross sections in Fig. 4 are normalized to the present theory). The somewhat larger theoretical ratio of the integral intensities of two channels is due to the assumption that the asymptotical jj representations of the total wave functions (2) are valid at all internuclear distances. Importantly, because of the dominant role of the $|^2\Sigma^+_{\pm1/2}\rangle$ basis state, the latter assumption does not affect the computed angular distributions $\beta(\omega)$.

D. Molecular-frame angular distributions for He + Ne^+ channel

More detailed information on the dynamics of the RICD process can be obtained by investigating the molecular-frame angular distributions of the emitted electrons. The body-fixed frame RICD electron angular distributions as obtained for He + Ne^+ fragmentation channel in the experiment exhibit, however, almost isotropic emission patterns for all peaks (not shown here for brevity). This observation supports the present assumption of a very slow dissociation creating these fragments, such that the measured intensities become completely averaged over all orientations of HeNe owing to molecular rotations (i.e., breakdown of the axial recoil approximation).

Nevertheless, such molecular-frame angular distributions are still accessible to our calculations. Figure 5 summarizes the angular emission patterns of RICD electrons in the frame of fixed-in-space dimers. These distributions were computed for the $A^2\Pi_{1/2}$ ionic state Eq. (2c), which represents the fragmentation channel. Here, the HeNe dimer lies within the plane perpendicular to the propagation direction of the linearly polarized synchrotron radiation and is oriented along the horizontal axis with the Ne^+ ion at the right-hand side. The electrons plotted are also emitted within that dipole plane. Each panel shows normalized angular distributions computed on the top of different vibronic resonances Nos. 1–6, as enumerated in the upper panel of Fig. 4 and in Table I.

The calculations were performed for different orientations of the polarization vector of the exciting radiation with respect to the molecular axis. In the case of its horizontal orientation (electric-field vector is parallel to the molecular axis), selection rules enable excitation of the $3d\sigma$ electronic state via a $\sigma \rightarrow \sigma$ transition (dashed curves in Fig. 5). On the contrary, only the $3d\pi$ and $3p\pi$ electronic states are accessible via $\sigma \rightarrow \pi$ transitions for the vertical orientation of the polarization vector (electric-field vector is perpendicular to the molecular axis, shown by dash-dotted curves). Averaging over all orientations of the polarization vector with respect to the molecular axis yields a result which is proportional to the sum of those two contributions (shown by solid black curves in Fig. 5, normalized to their maxima).

As one can recognize from Fig. 5, for peaks Nos. 1, 5, and 6, the partial contribution from the vertical orientation of the polarization vector is dominant (the solid and the dash-dotted curves in the respective panels are almost indistinguishable). This result is in agreement with the assignments of these resonances as being of pure π character (indicated in each panel). For peak No. 2, the horizontal orientation of the polarization vector provides the dominant contribution (the solid and the dashed curves in this panel are almost indistinguishable), which indicates a pure σ character of this resonance. For peaks Nos. 3 and 4, both orientations provide noticeable contributions, which is owing to the overlap of the lifetime-broadened resonances of both symmetries.

It is interesting to note that the molecular-frame angular distributions depicted in Fig. 5 provide a direct access to the symmetry of intermediate electronic resonances. Indeed, these emission distributions resemble the respective electron densities of excited electrons, which are additionally distorted by a positive charge on the Ne^+ side: i.e., of π electrons for peaks Nos. 1, 5, and 6; of σ electrons for peak No. 2; and of a mixture of both symmetries for peaks Nos. 3 and 4. This is because the angular emission distribution of RICD electrons in the fragmentation channel is governed by the electronic transition in the $|^2\Sigma^+_{\pm 1/2}\rangle$ basis state (see discussion in the preceding section).

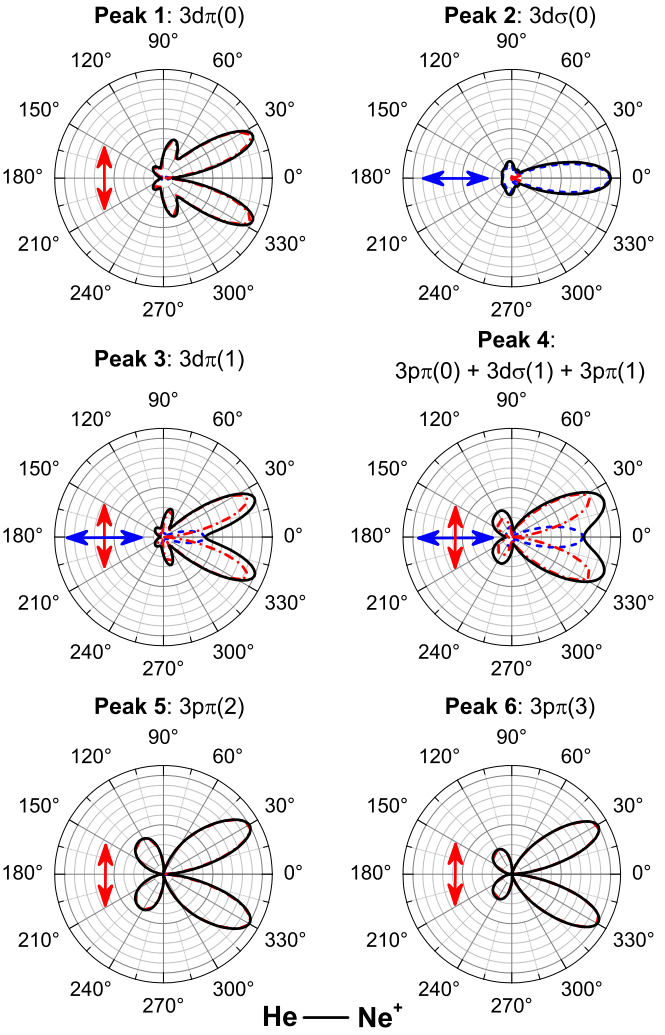

FIG. 5. Molecular-frame angular emission distributions of RICD electrons, computed for the selected resonances (indicated at the top of each panel together with the assignment from Table I). The electrons are emitted in the dipole plane of the linearly polarized synchrotron radiation (i.e., the plane perpendicular to the photon propagation direction). The dimer is also oriented in that plane along the horizontal axis with the Ne^+ ion pointing to the right, as indicated at the bottom. (Dash-dotted curves) The polarization vector is oriented vertically. (Dashed curves) The polarization vector is oriented horizontally. (Solid curves) Sum of the two contributions, which is proportional to the result of integration over all orientations of the polarization vector. Each solid black curve is normalized to its maximal value. For the peaks 1, 2, 5, and 6, the integrated angular emission distribution (solid curve) is almost identical to that obtained for one particular orientation of the light's polarization as indicated by the respective double arrow in the panels, and contribution from another orientation is very small.

VI. CONCLUSION

The emission of electrons due to resonant ICD in HeNe has been studied experimentally and theoretically in large detail. The experiment has been carried out employing synchrotron radiation using coincident detection techniques (COLTRIMS). For the $He^{20}Ne$ isotope of the dimer, two channels representing bound final ionic states $HeNe^+$ and a fragmentation into $He + Ne^+$ have been identified in the coincident time-of-flight spectrum. The bound channel corresponds to the population of all discrete vibrational states of the two lowest final ionic states $X^2\Sigma^+_{1/2}$ and $a^2\Pi_{3/2}$ of the $HeNe^+$ ion. It is suggested, that the fragmentation channel emerges due to an extremely slow homogeneous dissociation of the uppermost $A^2\Pi_{1/2}$ final ionic state into vibrational continua of the lower ionic states $X^2\Sigma^+_{1/2}$ and $a^2\Pi_{3/2}$. The very slow fragmentation results in the breakdown of the axial recoil approximation. As a consequence, the molecular-frame angular distributions of RICD electrons, observed in the coincident signal for the fragmentation channel, are completely washed out by the molecular rotation. The rotation of the molecule prior to its dissociation is an obstacle that cannot be overcome easily with experimental techniques routinely available nowadays. Active (adiabatic) molecular alignment techniques employing strong laser fields, for example, have so far not been extended to work in combination with high resolution synchrotron radiation, but might be a feasible pathway for future endeavours.

The laboratory-frame angular distributions of RICD electrons observed for both channels are interpreted by *ab initio* electronic structure calculations, performed using the single center method including underlying nuclear dynamics. The present theoretical interpretation relies on relativistic total wave functions (2) of the final ionic states in the jj-coupling scheme. Here, the main contribution to RICD is provided by the electronic transition into the $|^2\Sigma^+\rangle$ basis state, while the decay into the $|^2\Pi\rangle$ basis states is rather negligible. As a consequence, the computed integral intensities of the two channels, as well as the respective angular distribution parameters, are quite comparable and possess similar dependencies on the exciting-photon energy, which is in agreement with the experimental observations. The computed molecular-frame angular distributions of RICD electrons can be considered as predictions. These MFADs show a direct correspondence of the dipole-plane emission pattern to the symmetry of intermediate decaying vibronic states.

ACKNOWLEDGMENTS

This work was supported by the Deutsche Forschungsgemeinschaft within the Forschergruppe FOR 1789 and partly by the Förderprogramm zur weiteren Profilbildung in der Universität Kassel (Förderlinie *Große Brücke*).

[1] L. S. Cederbaum, J. Zobeley, and F. Tarantelli, Phys. Rev. Lett. **79**, 4778 (1997).
[2] S. Marburger, O. Kugeler, U. Hergenhahn, and T. Möller, Phys. Rev. Lett. **90**, 203401 (2003).
[3] T. Jahnke *et al.*, Phys. Rev. Lett. **93**, 163401 (2004).
[4] V. Averbukh *et al.*, J. Electron Spectr. Relat. Phenom. **183**, 36 (2011).
[5] U. Hergenhahn, J. Electron Spectrosc. Relat. Phenom. **184**, 78 (2011).
[6] U. Hergenhahn, Intl. J. Radiat. Biology **88**, 871 (2012).
[7] T. Jahnke, J. Phys. B **48**, 082001 (2015).
[8] T. Jahnke *et al.*, Phys. Rev. Lett. **88**, 073002 (2002).
[9] H. Sann *et al.*, Phys. Rev. Lett. **117**, 263001 (2016).
[10] N. A. Cherepkov and S. K. Semenov, J. Phys. B **37**, 1267 (2004).
[11] T. Jahnke *et al.*, J. Phys. B **40**, 2597 (2007).
[12] K. Kreidi *et al.*, J. Phys. B **41**, 101002 (2008).
[13] S. K. Semenov *et al.*, Phys. Rev. A **85**, 043421 (2012).
[14] T. Havermeier *et al.*, Phys. Rev. A **82**, 063405 (2010).
[15] F. Trinter *et al.*, Phys. Rev. Lett. **111**, 233004 (2013).
[16] G. Jabbari, S. Klaiman, Y. C. Chiang, F. Trinter, T. Jahnke, and K. Gokhberg, J. Chem. Phys. **140**, 224305 (2014).
[17] H. Sann *et al.*, Chem. Phys. **482**, 221 (2017).
[18] B. Najjari, A. B. Voitkiv, and C. Müller, Phys. Rev. Lett. **105**, 153002 (2010).
[19] A. Kramida, Y. Ralchenko, and J. Reader, NIST Atomic Spectra Database (National Institute of Standards and Technology, Gaithersburg, 2018), http://physics.nist.gov/PhysRefData/ASD/index.html.
[20] R. Dörner, V. Mergel, O. Jagutzki, L. Spielberger, J. Ullrich, R. Moshammer, and H. Schmidt-Böcking, Phys. Rep. **330**, 95 (2000).
[21] J. Ullrich, R. Moshammer, A. Dorn, R. Dörner, L. P. Schmidt, and H. Schmidt-Böcking, Rep. Prog. Phys. **66**, 1463 (2003).
[22] T. Jahnke, Th. Weber, T. Osipov, A. L. Landers, O. Jagutzki, L. Ph. H. Schmidt, C. L. Cocke, M. H. Prior, H. Schmidt-Böcking, and R. Dörner, J. Electron Spectrosc. Relat. Phenom. **141**, 229 (2004).
[23] W. C. Wiley and I. H. McLaren, Rev. Sci. Instrum. **26**, 1150 (1955).
[24] G. Schiwietz, M. Beye, and T. Kachel, J. Large-Scale Res. Facil. **1**, A33 (2015).
[25] N. A. Cherepkov, J. Phys. B **14**, 2165 (1981).
[26] N. A. Cherepkov, Chem. Phys. Lett. **87**, 344 (1982).
[27] T. G. Wright, B. R. Gray, L. A. Viehland, and R. Johnsen, J. Chem. Phys. **129**, 184307 (2008).
[28] H. Lefebvre-Brion, *Perturbation in the Spectra of Diatomic Molecules* (Academic Press, London, 1986).
[29] A. L. Roche and H. Lefebvre-Brion, Chem. Phys. Lett. **32**, 155 (1975).
[30] J. Tellinghuisen and D. L. Albritton, Chem. Phys. Lett. **31**, 91 (1975).
[31] F. K. Gel'mukhanov, L. N. Mazalov, and A. V. Kondratenko, Chem. Phys. Lett. **46**, 133 (1977).
[32] A. Cesar and H. Ågren, Phys. Rev. A **45**, 2833 (1992).
[33] V. Schmidt, Rep. Prog. Phys. **55**, 1483 (1992).
[34] Ph. V. Demekhin, I. D. Petrov, V. L. Sukhorukov, W. Kielich, P. Reiss, R. Hentges, I. Haar, H. Schmoranzer, and A. Ehresmann, Phys. Rev. A **80**, 063425 (2009); **81**, 069902(E) (2010).
[35] A. Knie, M. Ilchen, Ph. Schmidt, Ph. Reiß, C. Ozga, B. Kambs, A. Hans, N. Müglich, S. A. Galitskiy, L. Glaser, P. Walter, J. Viefhaus, A. Ehresmann, and Ph. V. Demekhin, Phys. Rev. A **90**, 013416 (2014).

[36] Ph. V. Demekhin, A. Ehresmann, and V. L. Sukhorukov, J. Chem. Phys. **134**, 024113 (2011).

[37] S. A. Galitskiy, A. N. Artemyev, K. Jänkälä, B. M. Lagutin, and Ph. V. Demekhin, J. Chem. Phys. **142**, 034306 (2015).

[38] A. N. Artemyev, A. D. Müller, D. Hochstuhl, and Ph. V. Demekhin, J. Chem. Phys. **142**, 244105 (2015).

[39] A. Ehresmann, L. Werner, S. Klumpp, H. Schmoranzer, Ph. V. Demekhin, B. M. Lagutin, V. L. Sukhorukov, S. Mickat, S. Kammer, B. Zimmermann, and K. H. Schartner, J. Phys. B **37**, 4405 (2004).

[40] Ph. V. Demekhin, D. V. Omelyanenko, B. M. Lagutin, V. L. Sukhorukov, L. Werner, A. Ehresmann, K.-H. Schartner, and H. Schmoranzer, Opt. Spektrosc. **102**, 318 (2007).

[41] A. Ehresmann, Ph. V. Demekhin, W. Kielich, I. Haar, M. A. Schlüter, V. L. Sukhorukov, and H. Schmoranzer, J. Phys. B **42**, 165103 (2009).

[42] Ph. V. Demekhin, V. L. Sukhorukov, H. Schmoranzer, and A. Ehresmann, J. Chem. Phys. **132**, 204303 (2010).

[43] Ph. V. Demekhin, I. D. Petrov, T. Tanaka, M. Hoshino, H. Tanaka, K. Ueda, W. Kielich, and A. Ehresmann, J. Phys. B **43**, 065102 (2010).

[44] Ph. V. Demekhin, I. D. Petrov, V. L. Sukhorukov, W. Kielich, A. Knie, H. Schmoranzer, and A. Ehresmann, Phys. Rev. Lett. **104**, 243001 (2010).

[45] Ph. V. Demekhin, I. D. Petrov, V. L. Sukhorukov, W. Kielich, A. Knie, H. Schmoranzer, and A. Ehresmann, J. Phys. B **43**, 165103 (2010).

[46] F. V. Demekhin, D. V. Omel'yanenko, B. M. Lagutin, V. L. Sukhorukov, L. Werner, A. Ehresmann, K.-H. Schartner, and H. Schmoranzer, Russ. J. Phys. Chem. B **1**, 213 (2007).